Available online at www.sciencedirect.com
ScienceDirect

DEEP-SEA RESEARCH
PART I

Deep-Sea Research I 55 (2008) 1–19

www.elsevier.com/locate/dsri

Coastal jet separation and associated flow variability in the southwest South China Sea

Jianping Gan[a,*], Tangdong Qu[b]

[a]Department of Mathematics and the Atmospheric, Marine and Coastal Environment Program, Hong Kong University of Science and Technology, Kowloon, Hong Kong, USA
[b]International Pacific Research Center, SOEST, University of Hawaii, Honolulu, USA

Received 3 May 2007; received in revised form 12 September 2007; accepted 19 September 2007
Available online 2 October 2007

Abstract

A three-dimensional, high-resolution regional ocean model, forced with high-frequency wind stress and heat flux as well as time- and space-dependent lateral fluxes, is utilized to investigate the coastal jet separation and associated variability of circulation in the southwest South China Sea (SSCS). It is found that the circulation and its variability in the SSCS are dominated by the flow fields and eddies associated with the southward and northeastward wind-driven coastal jet separation from the coast of central Vietnam in the winter and summer, respectively. As a result of the coastal jet separation, cyclonic and anticyclonic eddies with strong flow variability are generated in the regions to the southeast of the Vietnam in the winter and to the east off central Vietnam in the summer. The separation of the wind-driven coastal jet is largely associated with the formation of adverse pressure gradient force over the shallow shelf topography around the coastal promontory off central Vietnam, balanced mainly by wind stress in the summer and by both wind stress and nonlinear advection in the winter. In the vorticity balance, a bottom pressure torque, the force exerted on the wind-driven current by the shelf topography, tends to yield an adverse vorticity favorable for the separation of coastal jet. The results suggest that the interaction between wind-driven coastal currents and shelf topography in the nearshore waters plays a crucial role in controlling the separation of the coastal jet.

Keywords: South China Sea; Coastal jet separation; Numerical modeling; Circulation variability

1. Introduction

The circulation in the South China Sea (SCS) is driven mainly by Asian monsoonal atmospheric fluxes and lateral influxes that intrude from both the Luzon Strait (LS) and the Taiwan Strait (TS) in the north South China Sea (NSCS) and from the Karimata Strait (KS) in the southwest SCS (SSCS) (Wyrtki, 1961). Forced by the prevailing northeasterly and southwesterly monsoonal winds in the winter and summer, respectively, cyclonic and anticyclonic basin-scale circulations are typically formed by flows around the continental margin in the SCS. Eddies with different horizontal scales are embedded in these basin-scale circulations (Xu et al., 1982). Besides being driven by the monsoonal variation in the atmospheric forcing, the variability in SCS circulation is also largely governed by regional dynamics mainly involving Kuroshio intrusion in the

*Corresponding author.
E-mail address: magan@ust.hk (J. Gan).

0967-0637/$ - see front matter © 2007 Elsevier Ltd. All rights reserved.
doi:10.1016/j.dsr.2007.09.008

NSCS (Xue et al., 2004; Li et al., 1998) and the coastal jet formation in the SSCS (Shaw and Chao, 1994; Xie et al., 2003; Liu et al., 2004). These features have been identified by many investigators based on historical *in situ* hydrographic observations (e.g., Xu et al., 1982; Qu et al., 2000, 2007) and by modeling studies (e.g., Shaw, 1991; Metzger and Hurlburt, 1996; Chao et al., 1996; Chu et al., 1999; Xie et al., 2003; Gan et al., 2006). However, the spatial and temporal limitations of the existing hydrographic measurements and the general adoption of low horizontal (>20 km) and vertical (<30 levels) grid sizes in many previous modeling studies have precluded us from a more accurate description of the flow field and its variability in the SCS. In addition, processes induced by intrinsic dynamics in the circulation are rarely investigated.

Derived from the weekly sea surface height anomaly (SSHA) obtained from TOPEX/POSEIDON (T/P) data and the climate density field, as presented in Gan et al. (2006), Fig. 1 shows the values of the standard deviations (stds) of the geostrophic velocity vector amplitudes and of SSHA during the period July 2000 through June 2003. The variability in the circulation in the SCS is evidently characterized by the existence of strong variability in the waters west of the LS in the NSCS and in the SSCS. Much larger stds occur in the SSCS. A similar double center of the strong flow variability was obtained in the analysis of the time-domain empirical orthogonal function (EOF) of T/P altimetry data by Shaw et al. (1999). Their results showed that this double center covers 65% of the variance in the SCS that is ascribed to a symmetric reversal of the winter and summer circulation in the basin. The finding was later verified by a modeling study from a three-dimensional numerical model forced with $2.5^\circ \times 2.5^\circ$ NCEP/NCAR daily wind and sea surface temperature (SST) (Wu et al., 1998). Shaw et al. (1999) indicated that the southern center was caused mainly by the corresponding variance in the local wind field while the intrusion of the warm Kuroshio current may contribute to the variance in the northern center. These two regions of high stds were also identified by Qu (2000) who associated them with two corresponding local cyclonic eddies induced by a wind stress curl. Liu et al. (2001), using T/P and Levitus data as well as numerical and theoretical models, found that the seasonal circulation over most of the SCS basin is determined predominantly by the regional ocean dynamics,

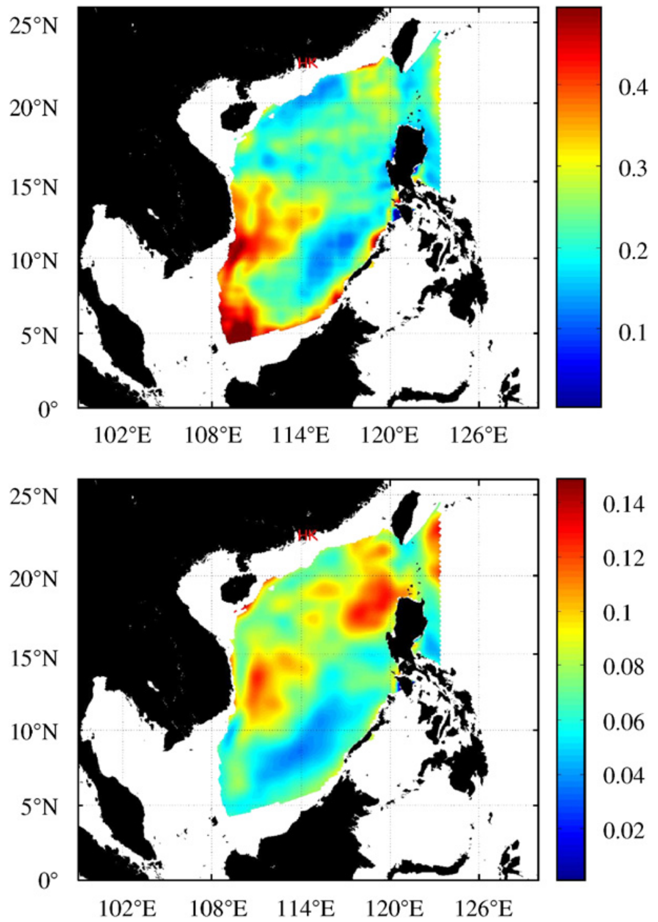

Fig. 1. Standard deviations of the surface geostrophic velocity vector amplitudes ($m\,s^{-1}$, upper panel) and of sea surface height anomaly (m, lower panel) derived from T/P data in the South China Sea for the period from July 2000 to June 2003.

particularly over the region in the SSCS. He et al. (2002), using three-year T/P altimetry data, showed that strong eddy kinetic energy (EKE) existed in the region west of the northern Philippine Islands in the NSCS in all seasons. The strongest EKE values were also identified in the regions to the east off central Vietnam in the summer and fall and to the southeast of the Vietnam coast in the winter. Although there have been many investigations of the flow field variation in previous studies, most attention has been given to the anomalies over year-long, interannual and longer time scales induced by the corresponding variation from monsoonal wind forcing. The same amount of attention has not been given to the variability in the flow field arising from intrinsic dynamics embedded in the circulation within seasonal time scale.

The boundary current separation is a phenomenon in which the current leaves the solid boundary which it has attached, overshoots and forms eddy in the interior (Batchelor, 1967). The offshore detaching of the coastal jet from the coast of Vietnam and the corresponding eddy formations in the SSCS during both summer (Shaw and Chao, 1994; Xie et al., 2003) and winter (Gan et al., 2006; Liu et al., 2004) are phenomena of coastal current separation (Haidvogel et al., 1992; Gan et al., 1997, 2004). The mechanism for current separation has been generally related to the formation of the adverse pressure gradient force, induced mainly by the intensified current (jet), wind forcing, coastal curvature, rotation and factors in boundary layer. In the SSCS, the jet separation in the SSCS in the summer has been generally ascribed to the existence of local dipole wind stress curl (Shaw and Chao, 1994; Xie et al., 2003) in which the coastal jet off the Vietnam coast tends to follow zero-wind-curl contour. The separation mechanism involving in the intrinsic dynamics of the wind-forced coastal jet, however, has not been investigated, which precludes a more completed understanding of flow field and its variability in the SCS. In the winter, separation of the southward coastal jet ($>0.5\,\mathrm{m\,s^{-1}}$) from the coast of central Vietnam has been shown as a distinct cold tongue separating the Sunda Shelf to the west and the deep SCS basin to the east (Liu et al., 2004). However, little attention has been paid on the dynamic processes involved in the southward coastal jet separation in the winter. The objectives of this study are, by using a three-dimensional ocean circulation model and available altimetry data to investigate the coastal jet separation and associated flow variability (Fig. 1) in the SSCS. Two key regions with existence of eddied, bound by the area within 10−15°N, 108−114°E (referred to as R1) in the north and within 4−10°N, 108−114°E (referred to as R2) in the south (Fig. 2), are to be focused.

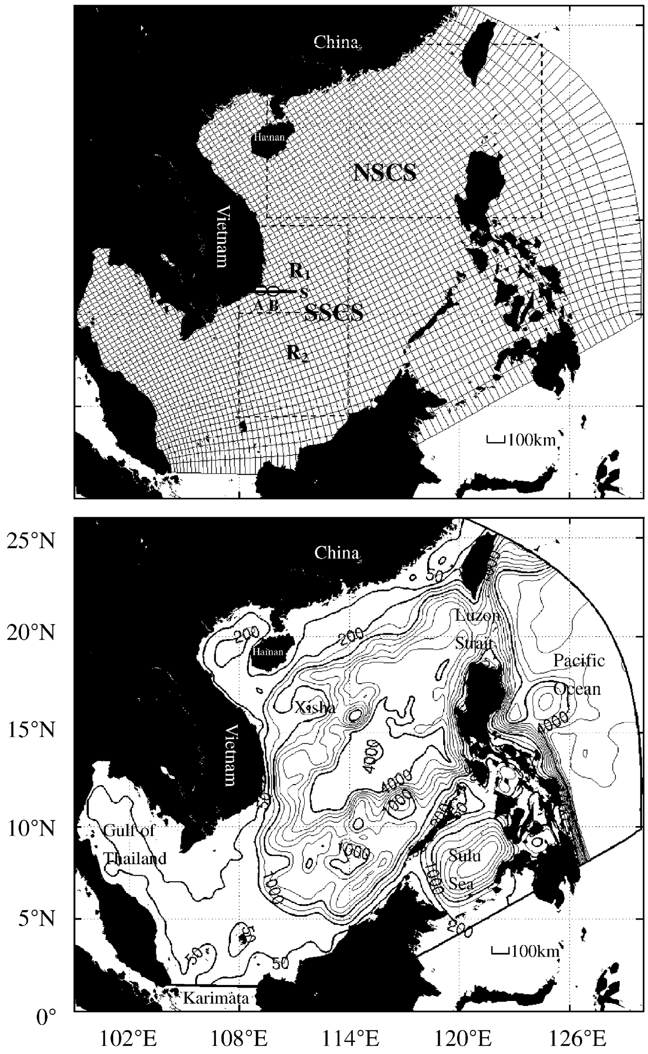

Fig. 2. The model's curvilinear grid and bathymetry with the 50, 200, 1000 and 4000 m isobaths shown as thicker lines. The contour interval for water deeper than 200 m is 500 m. One-third of the horizontal grid point is shown. The regions in SSCS with the sub-regions R1 and R2 as well as NSCS are marked. The location of the cross-section in the SSCS are labeled with line s.

2. The ocean model

The ocean model used is the Princeton Ocean Model (POM) (Blumberg and Mellor, 1987) for three-dimensional, time-dependent oceanographic flows governed by hydrostatic primitive equations. The model domain extends from 1.5°N to about 26°N in the north–south direction, and from about 100°E to 130°E in the east–west direction (Fig. 2). Unlike many previous studies, this model domain covers the region to the east of the Philippine Islands so that the Kuroshio dynamics can be better represented in the model. The numbers of grid points in the horizontal (x, y) and vertical (σ) directions are 259, 181 and 30, respectively. The horizontal grid spacing is variable, with small spacing (Δx, $\Delta y =$ about 10 km) in the northern and central parts of the domain and a much larger grid size (Δx, $\Delta y =$ about 20−30 km) in the eastern and southern parts of the domain. The bottom topography is obtained from ETOPO2 (1/30°) from the National Geophysical Data Center. The bathymetry is slightly smoothed to reduce truncation errors.

The SCS ocean model is initialized with the seven-year mean (1997–2003) winter (December-February) temperature (T) and salinity (S) from the Pacific Ocean model (Curchitser et al., 2005), which utilizes ROMS (Regional Ocean Modeling System;

Shchepetkin and McWilliams, 2005). The model is forced by daily NCEP (National Center for Environmental Prediction) reanalysis wind and flux products over a domain from 30°S–65°N and 100°E–70°W with a horizontal grid size of 40 km and 30 vertical levels. Although the ocean is shown to reach a statistical equilibrium after 500 days of integration (Gan et al., 2006), the SCS model continues to spin-up until day 1500. During the spin-up, the model is forced with the seven-year mean winter wind stress and heat flux calculated from NCEP data and with the seven-year mean winter lateral fluxes at the open boundaries obtained from the Pacific Ocean model. In addition, during the model spin-up, a relaxation correction term is introduced in the temperature equation at the surface ($\sigma = 1$) to relax the SST to the values obtained from the seven-year average MODIS (Moderate Resolution Imaging Spectroradiometer, NASA) SST in the winter. It takes the form,

$$\frac{\partial TD}{\partial t} + \frac{\partial TuD}{\partial x} + \frac{\partial TvD}{\partial y} + \frac{\partial T\omega}{\partial \sigma} = \frac{\partial}{\partial \sigma}\left(\frac{K_H}{D}\frac{\partial T}{\partial \sigma}\right) + F_T + \tau D(T^* - T), \tag{1}$$

where $D = H + \eta$ ($H =$ bottom topography and $\eta =$ surface elevation), ω is the vertical velocity in the σ coordinates, K_H is the vertical diffusive coefficient, F_T is the horizontal diffusion, τ is an inverse time constant that takes the value of one day at the surface ($\sigma = 1$) and zero elsewhere, T^* is the input field obtained from the seven-year average MODIS $0.25° \times 0.25°$ SST in the winter. Thus, the thermal flux at the surface during spin-up is controlled by both the observed SST and the atmospheric heat flux while the solar radiation is allowed to penetrate across the sea surface into the upper ocean. The salinity flux due to evaporation and precipitation is neglected in this study. After spin-up, the SST relaxation scheme is turned off and the model is then run in the hindcast mode forced with time-dependent six-hourly wind stress obtained from the $1 \times 1°$ NCEP data and lateral fluxes (three-day average values) of the Pacific model from 1 January 2000 to 30 June 2003. The confidence in NCEP wind data in the SCS is obtained by its similar features to $0.25 \times 0.25°$ daily QuickSCAT (NASA, USA) data. The surface heat flux is calculated from the bulk aerodynamic formula (Gan and Allen, 2005b) using the NCEP meteorological variables of the wind speed at 10 m, the surface air temperature, the relative humidity at 2 m, the cloud cover, the sea level pressure at a $1 \times 1°$ resolution and the six-hourly shortwave radiation retrieved from NCEP Reanalysis 1 with a $2.5° \times 2.5°$ resolution. Small values ($30\,\mathrm{m^2\,s^{-1}}$) of horizontal viscous and diffusive coefficients are adopted. Outputs from the last three years (July 2000–June 2003) of simulated results, archived every seven days, are used in the analysis.

Since the SCS is greatly influenced by the lateral momentum and buoyancy fluxes through LZ, TS and KS, the success of the simulation is largely dependent on the performance of the open boundary conditions (OBCs) that integrate the lateral fluxes into the SCS and allow the disturbances inside the domain to travel outward across the open boundary. The OBCs developed by Gan and Allen (2005a) are utilized as described in Appendix A.

3. Variability in circulation

3.1. *Surface flow field*

The three-year averaged surface geostrophic velocity vectors and the stds of the vector amplitudes ($\mathrm{m\,s^{-1}}$) in the winter (December–February), spring (March–May), summer (June–August) and fall (September–November) from the model are shown in Fig. 3. The geostrophic current is defined by

$$u_{gi} = (-1)^{1-i}\left(\frac{g}{f}\frac{\partial \eta}{\partial x_i}\right) + \frac{gD}{f\rho_0}\int_\sigma^0 \left(D\frac{\partial \rho'}{\partial x_i} - \frac{\sigma'}{D}\frac{\partial D}{\partial x_i}\frac{\partial \rho'}{\partial \sigma'}\right)\mathrm{d}\sigma', \tag{2}$$

where the geostrophic velocities (u_{gi}) in the east–west (x) and north–south (y) directions are represented by the subscripts $i = 1$ and 2 in the variables, respectively. The water density is ρ and the reference density is ρ_0. The corresponding stds of the vector amplitudes of surface geostrophic velocity are derived from weekly T/P SSHA data and Levitus $1 \times 1°$ gridded monthly climate temperature and salinity data (Gan et al., 2006). The model-observation comparison shows that std fields as well as circulation from simulation compare favorably with the observed fields, as also shown in Gan et al. (2006). It establishes a level of confidence in the flow field and variance contained in the simulated flow fields. To determine the governing process in the flow field, the total surface velocity

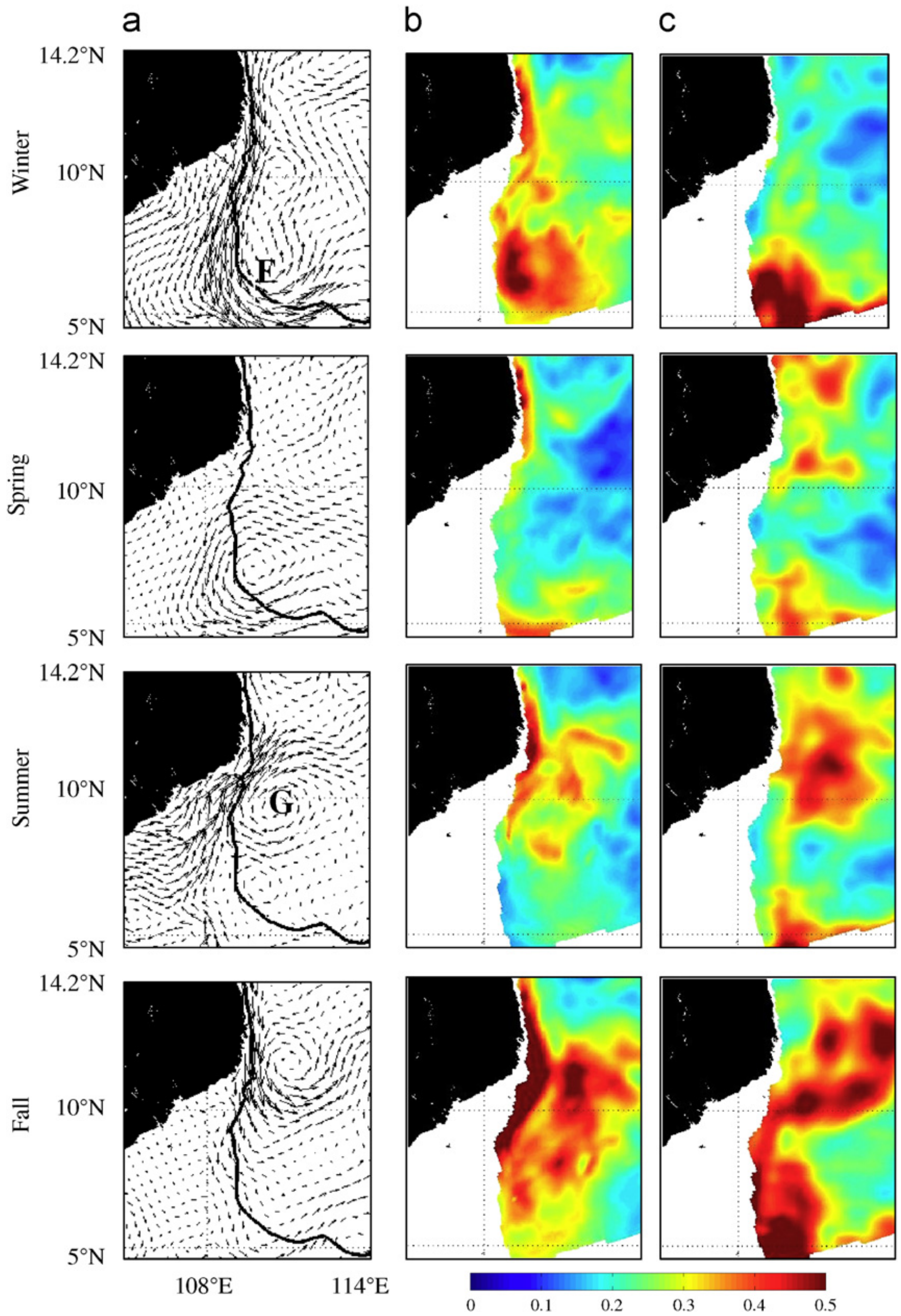

Fig. 3. Three-year mean seasonal (a) surface geostrophic velocity vectors ($m\,s^{-1}$) with heavy contour lines for the 200 m isobath. (b) std of surface geostrophic vector amplitudes ($m\,s^{-1}$) obtained from simulation, and (c) std of surface geostrophic velocity vector amplitudes ($m\,s^{-1}$) derived from the T/P data in the SSCS.

vectors (**v**) and the ageostrophic velocity vectors ($\mathbf{v}_a$), defined as the difference between (**v**) and the geostrophic velocity ($\mathbf{v}_g$), are also presented in Fig. 4.

The surface flow fields (Figs. 3 and 4) in the SSCS are characterized by the separation of the coastal jet from the coast of Vietnam and eddy formations in R1 and R2. In the winter, the southward coastal current off eastern Vietnam is intensified between 12°N and 14°N, mostly because of the narrowed shelf, the near-surface onshore flux from the interior of the SCS and the presence of local negative wind stress curls nearshore (see Section 4). The onshore flux is part of the cyclonic gyre over the entire southern basin induced by the winter wind stress curl (Shaw et al., 1999). Consequently, the accelerating coastal jet overshoots southward into R2 as it encounters the coastal promontory at about 12°N

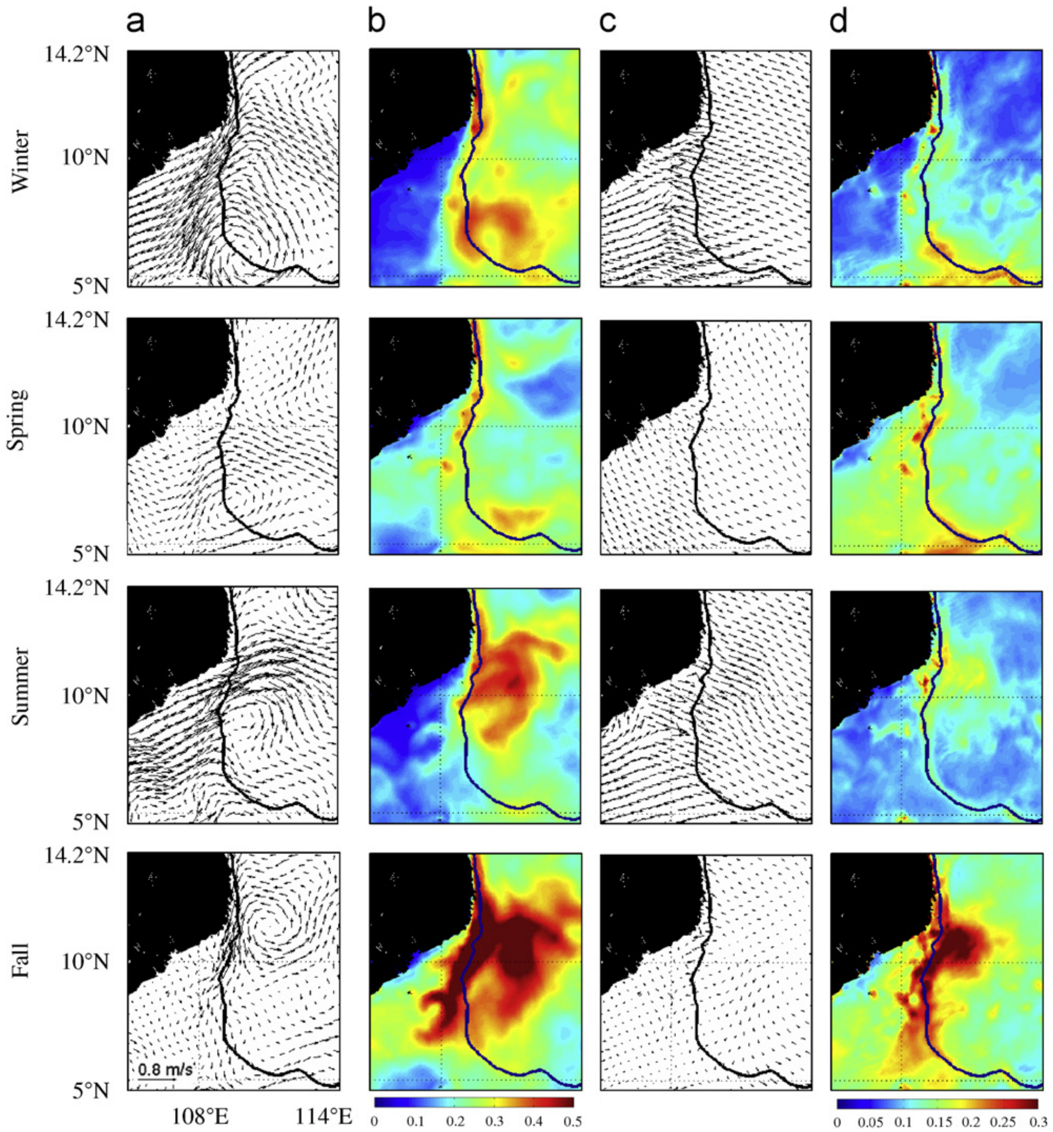

Fig. 4. Three-year mean seasonal (a) surface velocity vectors, (b) std of surface velocity vector amplitudes (m s^{-1}), (c) corresponding surface ageostrophic velocity vectors and (d) std of surface ageostrophic velocity vector amplitudes (m s^{-1}) from simulation in the SSCS.

and forms a cyclonic eddy (*F*). In the spring of the winter-to-summer transition period, the southward coastal current becomes invisible and eddy *F* is markedly weakened. In the summer, a northeastward coastal jet, driven mainly by the southeasterly monsoonal wind stress over the shelf in the southern part of Vietnam, separates from the coast at about 12°N and forms an anticyclonic eddy (*G*) in R1. This separated coastal current flows northeastward into the interior of the SCS and bifurcates around 113°E. The northern branch tends to meander toward the northeastern SCS while the southern one forms the anticyclonic eddy *G*, similar to the findings in hydrographic measurements by Fang et al. (2002). At the same time, a relatively small component of the coastal jet continues to flow northward, attaching to the coast off central Vietnam. This non-separated component of the coastal jet is strong when jet separation is weak. In the fall, the northeastward jet disappears as the onset of the northeasterly monsoon shifts the circulation from the summer regime to the winter one, starting from the NSCS (Gan et al., 2006). During this season, the strengthening southward coastal jet overshoots southeastward around 12°N and forms a cyclonic eddy in the north while the northeastward currents are quickly weakening in the south. A portion of the southward current is able to penetrate farther southward following the 200 m isobath in this season. The existence of the northward and southward coastal jets and eddies in the region was also identified in modeling studies (e.g., Shaw and Chao, 1994; Metzger and Hurlburt, 1996) and in field measurements (Chu et al., 1998; Fang et al., 2002; Qu et al., 2000). By comparing surface $\mathbf{v}_g$ (Fig. 3) and $\mathbf{v}$ (Fig. 4), we found that the surface $\mathbf{v}$ is contributed largely by $\mathbf{v}_a$ of a surface Ekman drift. In the winter, strong westward $\mathbf{v}_a$ in the southward jet is strengthened and tends to shift the jet westward crossing the isobath in R2 after the separation. In the summer, strong eastward $\mathbf{v}_a$ on the offshore side of the 200 m isobath near 12°N forms the eastward flows and enhances the separation of the jet from the coast. The surface $\mathbf{v}_a$ is weak in both spring and fall as a result of small wind magnitude. The analysis suggests that the jet separation near the coastal promontory in the surface waters can be modulated by the wind-induced $\mathbf{v}_a$ in the SSCS. Chu et al. (1999) found that the maximum surface Ekman current around 12°N has magnitudes of 0.43 m s^{-1} in the winter and 0.14 m s^{-1} in the summer.

The surface circulation in the SSCS has strong variability, both within each individual season (Fig. 4) and in the three-year-long time scale (Fig. 5). The three-year-long stds of the velocity vector amplitudes and of the SSHA from simulated fields (Fig. 5) agree reasonably well with the corresponding observed fields in Fig. 1. It clearly shows strong current variability in R1 and R2 as well as west of the LS. In the three-year-long time scale, the variability in the flow field contains seasonal variation, while std value in each season (Fig. 4) reflects the variability induced within each season. As shown in Figs. 3 and 4, larger stds are located in the regions along the jet, around eddy *G* in R1 in the summer and around eddy *F* in R2 in the winter. In the fall, strong variability occurs around the anticyclonic eddy in R1 and in the region over the northern part of R2 along the southward penetrating jet. A relatively stable flow field is found over the entire SSCS in the spring. Both velocity and its std fields conceivably suggest that the large flow variability in the SSCS occurs mainly along the track of the jet and in the regions where the eddies associated with separation are located. Relatively large stds in $\mathbf{v}_a$ occur in the same places as those in $\mathbf{v}$. Contributions of the stds from $\mathbf{v}_a$ to $\mathbf{v}$ in the surface are larger in the seasonal transition periods in the spring and fall, despite the small mean magnitudes of $\mathbf{v}_a$. Although the simulated results, both flow fields (Gan et al., 2006) and their stds (Fig. 3) in the surface, agree reasonably well with those derived from the altimetry data and climate

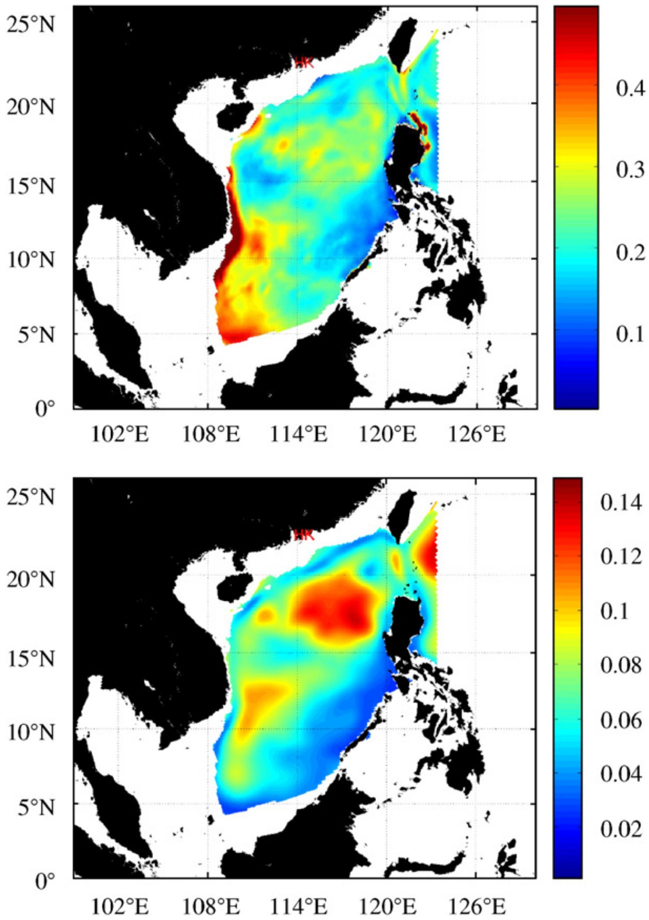

Fig. 5. Standard deviations of the surface geostrophic velocity vector amplitudes (m s^{-1}, upper panel) and of sea surface height anomaly (SSHA) derived from model outputs during the period between July 2000 to June 2003.

density field, some discrepancies inevitably exist. These differences have many possible causes, including the unrealistic representation of the climate density field in the $\mathbf{v}_g$ calculation, smoothed observational estimates, lower accuracy of the altimetry data near the coast, effects from the Mekong River outflow and others.

3.2. Depth-dependent alongshore transport

The velocity fields averaged from the upper 200 m and their corresponding std fields (Fig. 6) are qualitatively similar to those at the surface. However, as the wind effect is weakened with increasing water depth, the jet behaves more like $\mathbf{v}_g$. The eastward shifting of the jet is visibly weaker than the surface one in the summer while the southward jet is more southerly, following the shelf topography, in the winter. In deep waters, stds are small over entire SSCS in all seasons (not shown).

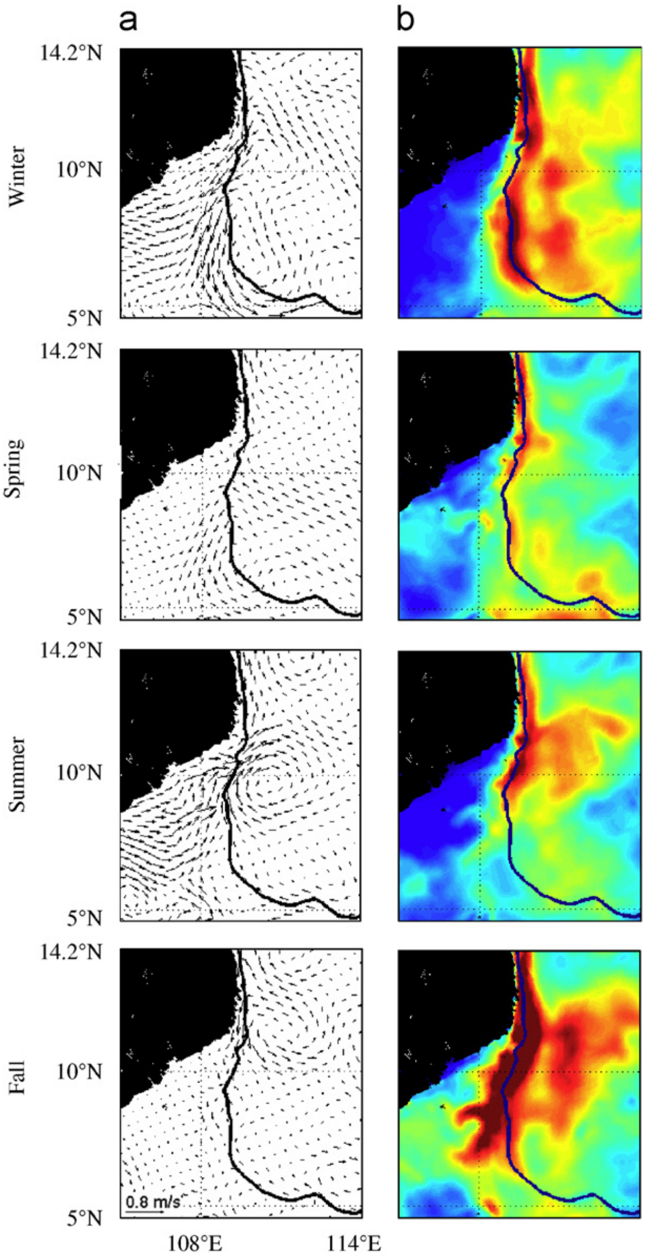

Fig. 6. Three-year mean seasonal (a) velocity vectors averaged over the upper 200 m and (b) std of velocity vector amplitudes ($m\,s^{-1}$) averaged over 200 m from simulation in the SSCS.

Depth-dependent characteristics of the coastal jet can be illustrated by the velocity profile (Fig. 7) normal to cross-shelf section s in R1 (Fig. 2). In the winter, the broad and strong southward coastal jet extends to the depths of 500 m nearshore and 200 m offshore. This jet accelerates northward toward the spring and forms a strong northward jet in the upper 200 m in the summer. The northward coastal jet then decelerates from the summer toward the fall and becomes southward in the upper 100 m in the fall. The core of the stronger coastal current is generally located about 100 km offshore over the upper 200 m, in which the horizontal velocity shear yields negative and positive vorticity on the shore-side of the core in the winter and summer, respectively. Currents are directed southward below the upper layer over the upper slope while alternative northward and southward currents are found in waters below 500 m in all seasons. Large stds are found in the jet over the upper 200 m, matching the results from measurements in the region (Fang et al., 2002). Relatively high std with larger vertical extension in the fall reflects the accelerating and deepening of the southward jet in the SSCS as circulation in the SCS is shifting from the summer to the winter regimes (Gan et al., 2006).

The time series of total monthly transport normal to s averaged over three years (Fig. 7) shows that the transport over the water column is predominantly directed northward except in the winter. In the upper 200 m representing the main body of the coastal jet, the transport accelerates northward from early March to August and southward from late September to December. The maximum northward and southward transport of about 5 Sv occurs in August and December, respectively. At depths between 200 m and 1500 m, the transport is directed northward without clear seasonal signals. The northward transport at depth may be contributed by the deep upwelling over the continental margin off Vietnam, which subsequently seeps into the coastal region (Chao et al., 1996). Obviously, the penetration of the currents from NSCS into the SSCS occur in the upper layer in the winter as also exhibited in the tracks of surface drifters (Gan et al., 2006).

4. Correlations with wind forcing and the jet separation

It has been known that wind stress in the coastal water or the wind stress curl itself is able to form a divergence of the Ekman flux and leads to the set-up of pressure gradients and the geostrophic currents. Consequently, the flow variability can arise from the variability in the wind forcing. Since the basin-wide circulation in the SCS is driven mainly by monsoonal wind stress (Wyrtki, 1961), it is fairly reasonable to expect that the variability of circulation in the upper ocean is controlled by the variation in the monsoonal wind stress field (Shaw et al., 1999). In the SSCS, the strong flow variability is

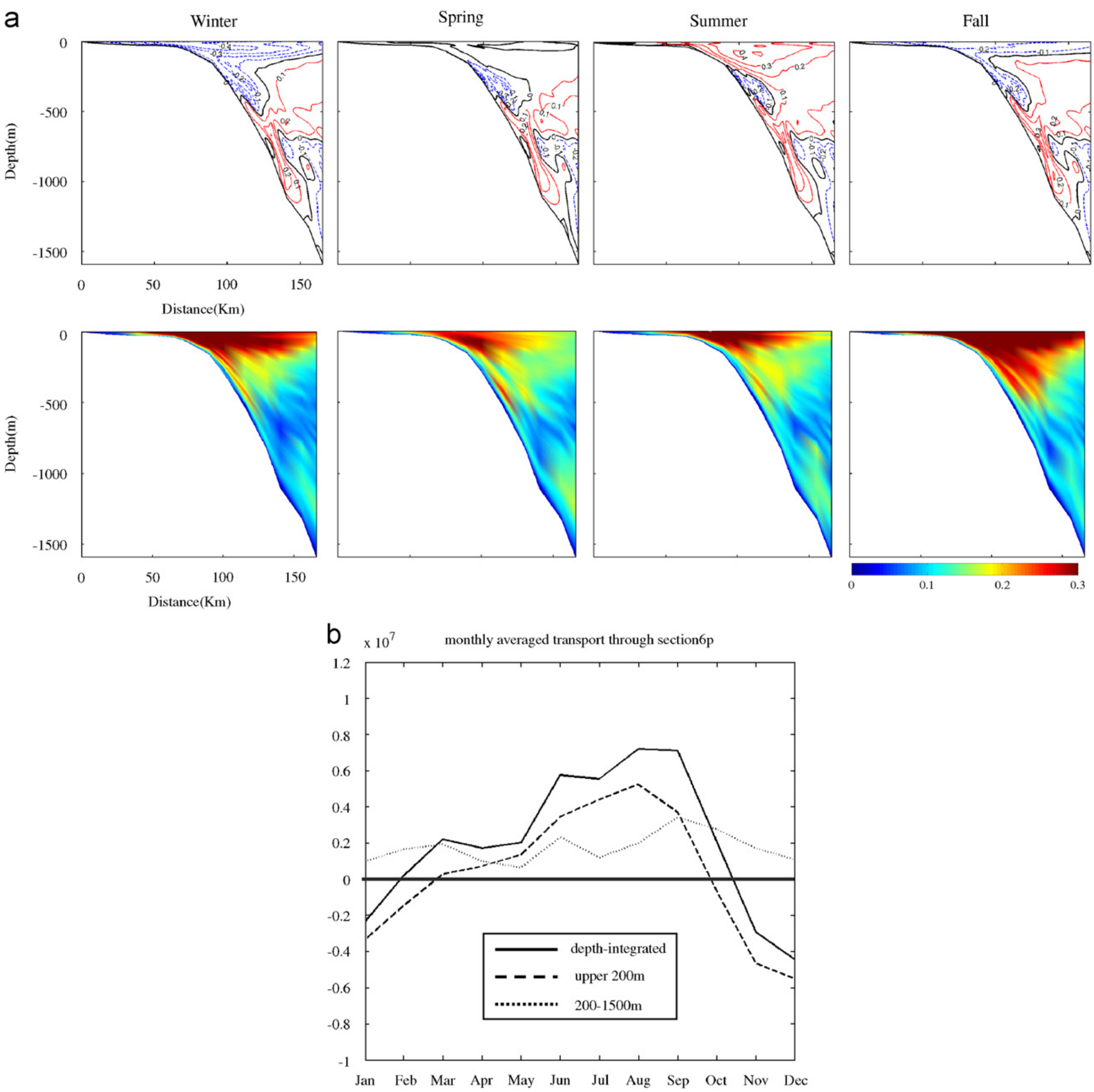

Fig. 7. (a) Three-year mean seasonal velocities (ms^{-1} upper row) normal to the cross-section *s* and their std values (lower row), (b) time series of three-year mean transport (m^3 s^{-1}) at different depths normal to section *s*. The positive values refer to the northward currents or transport.

expected to be imparted from the wind variability, since the dominant circulation, jets and their separations, is controlled largely by the wind fields (e.g., Xie et al., 2003). On the other hand, it is reasonable to speculate that the flow variability in the SSCS can also arise from the intrinsic dynamic processes associated with the jet separation and eddy formations.

4.1. Variability imparted from winds

Fig. 8 shows the three-year mean values of the wind stress curl and the stds of the vector amplitudes for both the wind stress curl and wind stress. The field of the wind stress curl in R1 is characterized by a large negative wind stress curl with large std in a band next to the coastline of

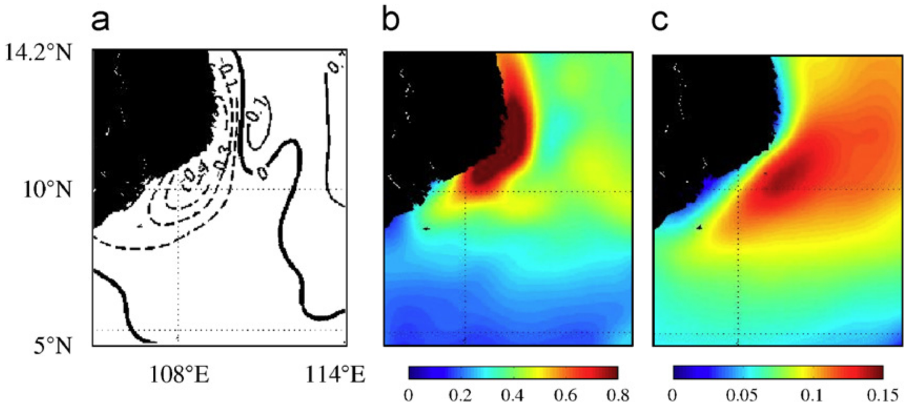

Fig. 8. (a) Three-year mean value wind stress curl (10^{-6} Pa m^{-1}), (b) the std of wind stress curl vector amplitudes (10^{-6} Pa m^{-1}) and (c) the std of wind stress vector amplitudes (Pa) in the SSCS.

Vietnam north of 8 °N, while a large std of the wind stress vector amplitudes exists farther offshore. In contrast, the wind stress curls and their stds are small in R2. The correlation of the stds between the wind and the current fields (Figs. 1 or 5) suggests that the variability in the wind field could contribute to the flow variability in R1 and along the track of the jet next to the coast, and there is no direct correlation between them in R2.

In each season, the wind stress curls and the wind stress fields also exhibit strong variability (Fig. 9) with strong correlation with the flow filed in R1, very similar to the conditions in the three-year-average field. Except in the summer, the spatial structures of wind stress curls have same pattern as that in the three-year-average field. An unique dipole wind stress curl with relatively large std values is shown in the summer. The orientation of the zero-wind-curl contour tends to be aligned with the track of the northeastward separated jet in R1 (Figs. 3 and 4). The stds of the wind stress curl in the summer have the smallest magnitude of all seasons, implying relatively stable conditions in the dipole wind stress curl. Similar to the three-year-long fields, the variability of the wind stress curls is small in R2 and the std of the wind stress is strong in the waters farther offshore from the coastal region in R1 in all seasons.

The correlations between the std wind fields and corresponding velocities in Figs. 3, 4 and 6 suggest that the variances in both the wind stress and curl can contribute to temporal variability in the near surface currents offshore while the source of variability in the coastal jet may be provided by the large variability in the wind stress curl next to the coast. No direct correlation of variability between the wind and the flow fields exists in R2. Clearly, source other than those from wind fields must also contribute to the variability in the flow field. Given that the high stds in R1 and R2 coincide with the locations where the coastal current separation and eddy formation occur, it is logical to investigate the possible flow variability induced by these processes.

4.2. *Variability induced by the jet separation*

The flow variability induced by the processes in the coastal jet separation as well as the role that the wind conditions play in these processes are investigated by additional numerical experiments forced with steady and curl-free wind stress fields in the winter and summer. In these experiments, the winter and summer cases are run separately and forced with the seven-year (1997–2003) mean atmospheric heat fluxes calculated from NCEP Reanalysis data and with the corresponding lateral fluxes provided by the Pacific Ocean model. The spatially uniform northeasterly wind stress in the winter and southwesterly in the summer of about 0.07 Pa, comparable to the magnitude of annual mean wind stress in the region, are adopted as the curl-free steady wind stress fields for these two cases. The model is run for 600 days, and the mean fields from the last 100 days are used for the analysis.

Fig. 10 shows the mean circulations and the std of the velocity vector amplitudes averaged over the upper 200 m. In the winter case, the southward coastal current and its separation are not visible, presumably because of the weak coastal jet due to the absences of the negative wind curl next to the coast of Vietnam (Fig. 9) and the weak onshore flux from large-scale circulation in the basin. Under this condition, the coastal currents tend to attach to the

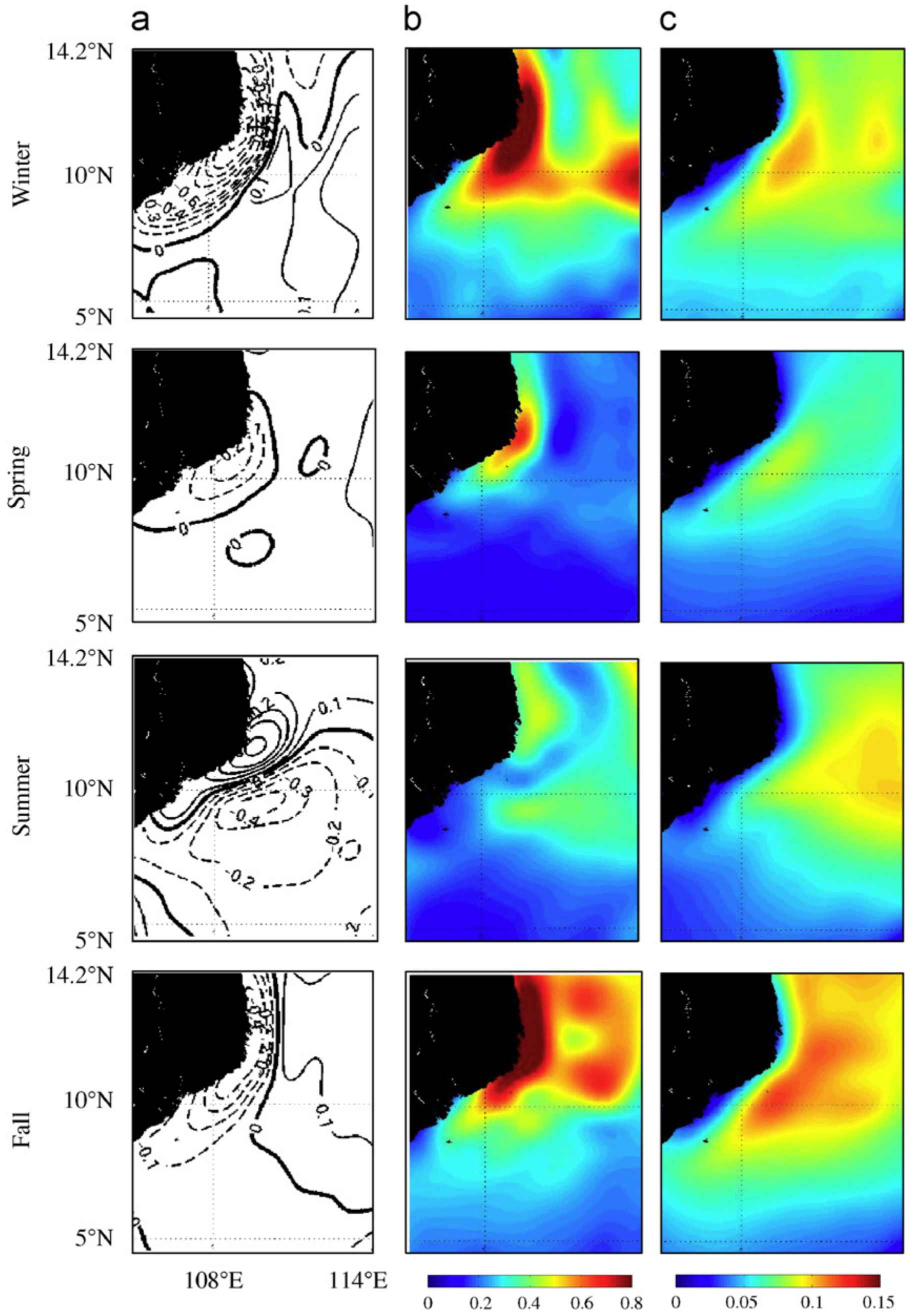

Fig. 9. (a) Three-year mean seasonal wind stress curl (10^{-6} Pa m^{-1}), (b) the std of wind stress curl (10^{-6} Pa m^{-1}) and (c) the std of wind stress vector amplitudes (Pa) in the SSCS.

coast and flow into the Gulf of Thailand without separation. Accordingly, the high std around eddy *F* in the standard case disappears. Interestingly, results from an experiment in which the magnitude of the winter wind stress is doubled (0.14 Pa) (Fig. 10), shows that a strong coastal jet separates from the coast of Vietnam and a cyclonic eddy is formed in R2, even when the wind curl is absent. More importantly, a large std in the flow field is found in R2 similar to the standard case in the winter. The dramatic difference in the cases with and without doubling the wind stress magnitude can also be seen in R_0 which is defined as the vorticity averaged over the upper 200 m divided by the Coriolis parameter. The R_0 is equivalent to the Rossby number but has a better representation of nonlinearity arising from velocity shear. It measures the ratio of the total flow to the flow with complete geostrophy. As expected, the values of R_0 are generally less than one, indicating the dominant role of geostrophy. With a doubled wind stress magnitude, both R_0 and its variability are enhanced

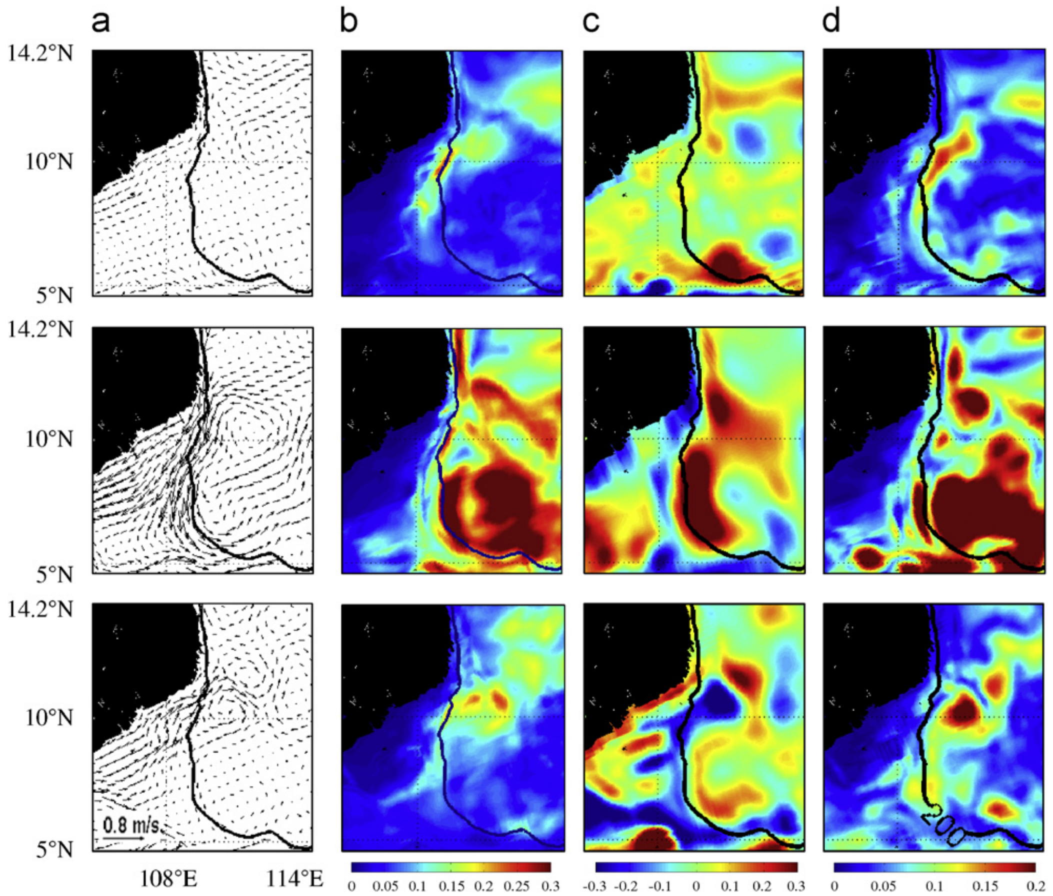

Fig. 10. Upper 200 m average of 100-day mean (a) velocity vectors (m s^{-1}), (b) std of velocity vector amplitudes (m s^{-1}), (c) vorticity divided by the Coriolis parameter (m s^{-2}) and (d) std values of vorticity divided by the Coriolis parameter (m s^{-2}) forced with zero wind stress curls for the cases of the winter (top row), of doubling wind stress magnitude in the winter (middle row) and of the summer (bottom row).

in R2, where the cyclonic eddy is located. Given that the winter monsoon is the strongest in all seasons in the SCS (i.e. >0.07 Pa of annual mean), the findings prove that the flow variability in R2 in the winter is induced by the cyclonic eddy associated with the southward separated coastal jet. Therefore, it is also conceivable that although there is no direct variability imparted from winds into the R2 region in the standard case, the high std in negative wind stress curl next to the coast between 8 °N and 14 °N will indirectly affect the flow variability in R2 by modulating the strength and separation of the southward jet.

In the experiment in the summer (Fig. 10), characteristics of the flow field obtained from the steady and the curl-free wind stress forcing are very similar to those in the standard case in Fig. 3. Both the coastal jet separation and the strong variability in the flow field around R1 exist even when the temporal and spatial variability in the wind stress field is removed. A strong cyclonic eddy in R1, represented by a large value of negative R_0, forms a large std in both velocity and R_0 fields. Thus, dynamic processes involved in the separation of boundary current (e.g., Gan et al., 1997) alone can also lead to the detachment of the coastal current from the coast. Huwang and Chen (2000), using the coherence analysis of EKE, the wind stress and the wind stress curl, also found that a local dynamic force other than the local wind field was responsible for the northeastward shifting of the alongshore currents when the wind in central Vietnam was almost westward.

5. Momentum and vorticity balances

The flow field and its variability in the SSCS are evidently associated with the processes in coastal jet separation. Thus, it is important to identify the forcing mechanisms that govern the coastal jet separation. In this section, analyses of momentum and vorticity balances are used to conduct the investigation. The depth-dependent momentum equations can be written as

$$\overbrace{\frac{\partial u_i D}{\partial t}}^{1}+\overbrace{\sum_{j=1,2}\frac{\partial u_i u_j}{\partial x_j}+\frac{\partial u_i \omega}{\partial \sigma}-F_i}^{2}+\overbrace{(-1)^i f u_i D}^{3}\overbrace{-\frac{\partial}{\partial \sigma}\left(\frac{K_M}{D}\frac{\partial u_i}{\partial \sigma}\right)}^{4}$$
$$\overbrace{+gD\frac{\partial \eta}{\partial x_i}+\frac{gD^2}{\rho_0}\int_\sigma^0\left(D\frac{\partial \rho'}{\partial x_i}-\frac{\sigma'}{D}\frac{\partial D}{\partial x_i}\frac{\partial \rho'}{\partial \sigma'}\right)\mathrm{d}\sigma'}^{5}=0, \tag{3}$$

where the momentum equations are rotated from model curvilinear coordinates to be directed in the east–west (x) and north–south (y) directions, represented by the subscripts $i=1$ and 2 in the variables, respectively; F_i is the horizontal viscosity term; ω is a velocity normal to σ surfaces; and K_M is the vertical turbulent viscosity coefficient. Terms in (3) are normalized by water depth, H, and are referred to as the (1) acceleration, (2) nonlinear advection and diffusion (NL), (3) Coriolis force (COR), (4) vertical diffusion (DIFF) and (5) pressure gradient (PRE). It is also convenient to consider the behavior of the sum of the COR and PRE, which is referred to as the ageostrophic pressure gradient (AGE).

5.1. Momentum balance and adverse pressure gradient

The time series of the three-year-average terms in the depth-integrated equations of (3) is first presented. Stations at water depths of 100 m over shelf (station A) and at 200 m near the edge of shelf (station B) along s (Fig. 2), representing the respective locations over the shelf and at the edge of shelf, are selected to identify the forcing processes of the summer northeastward and the winter southward coastal jet separation. The depth-integrated terms are represented with the same symbols as those in the depth-dependent equations but with lower-case letters. In addition, DIFF is replaced with surface stress, ts, and bottom stress, tb, in the depth-integrated form of (3). As reflected in x and y balances (Fig. 11a1, b1) at both stations, the coastal jet is primarily geostrophic. Mainly northward currents at A and northeastward currents at B, as represented by the corresponding cor_x and cor_y, start in early April and strengthen toward mid-August. The coastal jet, still dominated by the geostrophic balance, then decelerates in mid-October, becomes southwestward toward January and nearly southward afterward. Same as the cross-section velocity profiles (Fig. 7), the intensity of the coastal jet is much stronger at B near the shelf edge (Fig. 11a1 vs. Fig. 11b1). In contrast, ageostrophic currents, represented by age, has much larger value at A.

In the x direction at both A and B, the negative (eastward) wind stress, ts_x, is balanced by positive nl_x and age_x at both stations from late spring to early fall (hereafter referred to as Period 1). The age_x turns negative and stronger from early fall to late spring (referred to as Period 2), which balances the nl_x and ts_x. In the y direction, the ageostrophic balances are generally similar to the natures in the x direction but with smaller magnitudes (Fig. 11a3, b3). These results show that the northeastward wind stress at A and nearly eastward wind stress at B play major roles in their respective momentum balances during Period 1. Since the pressure gradients are positive in both x and y directions at A during Period 1 (Fig. 11a1), the corresponding positive age_x and age_y in Fig. 11a2, a3 represent a net southwestward pressure gradient force. This pressure gradient force, balanced by northeastward wind stress, is directed opposite to the northeastward jet and thus serves as an adverse pressure gradient force favorably for the coastal jet to separate (Batchelor, 1967; Signell and Gyer, 1991; Gan et al., 1997). Similarly, the northeastward adverse pressure gradient force is directed opposite to the southwestward jet at A in Period 2, but is balanced by both wind stress and nonlinear advection. Thus, the adverse pressure gradient force drives an adverse flow over the narrow shelf, which tends to deter the jet and cause the shear layer between the jet and coast to be pushed toward the mainstream of the jet so that the jet separates from the coast. Clearly, the adverse pressure gradient force varies with the wind stress in the northeastward separation of the coastal jet during Period 1, while both wind forcing and momentum advection lead to the formation of the adverse pressure gradient force in the southward separation of the coastal jet during Period 2. At B away from the shear layer between jet core and coast, the age terms are very small, and the adverse pressure gradient force is not so obvious. Thus, the formation of the adverse pressure gradient force is sensitivity to the shelf topography and the separation of the coastal jet is associated with the set-up of adverse pressure gradient force by the monsoonal wind stress in the shear layer between jet core and coast over the shallow shelf bottom topography.

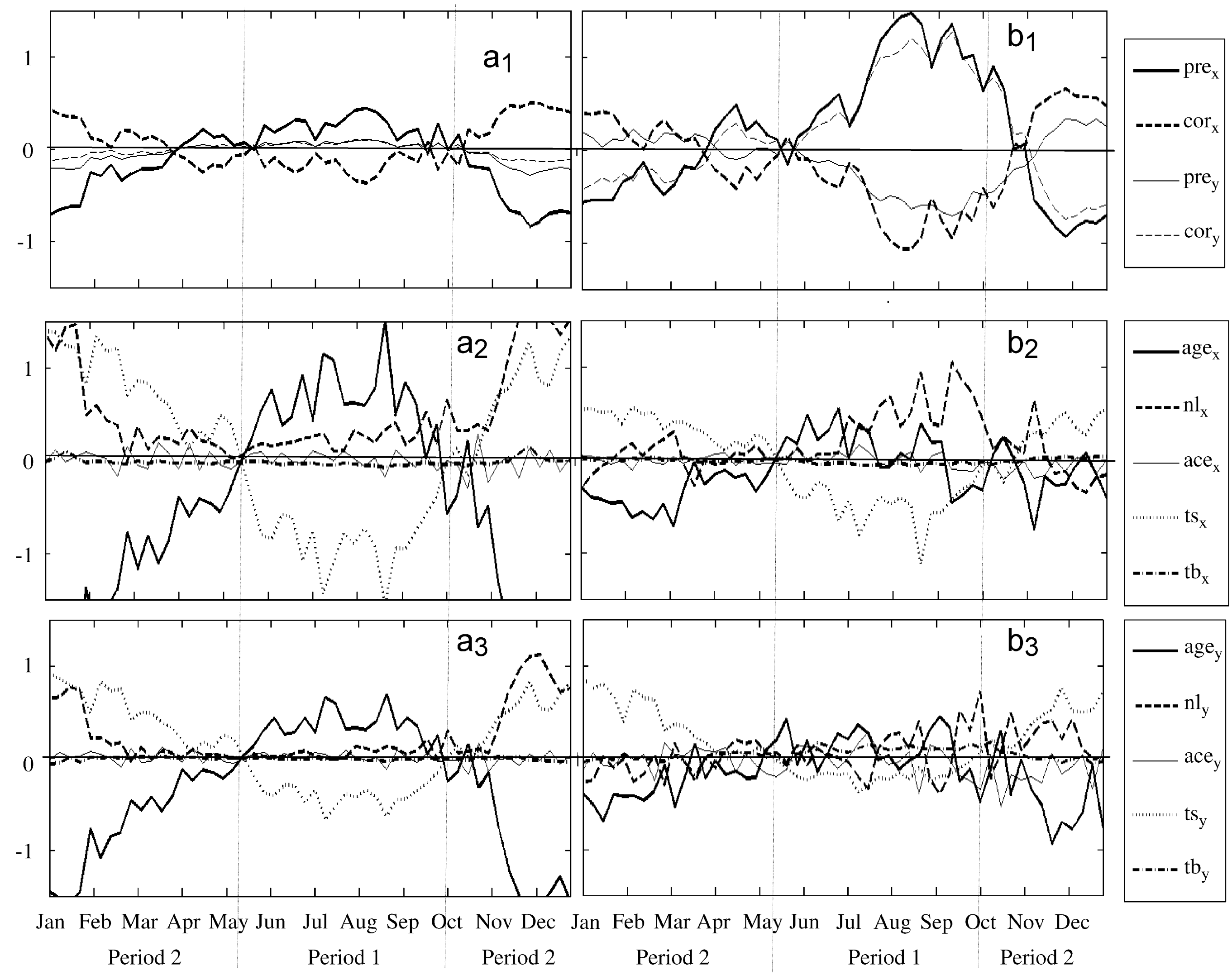

Fig. 11. Time series of three-year average pressure gradient pre, Coriolis force cor, ageostrophic term age, acceleration ace, nonlinear advection nl, surface wind stress ts and bottom stress tb in the depth-averaged momentum equations in both x and y directions (m s^{-2} multiplied by 10^5 for pre and cor and by 10^6 for the rest of the terms and divided by water depth) at station A (water depth 100 m) and B (water depth 200 m).

5.2. Vorticity balance and adverse vorticity

Effects of shelf topography on the separation of the coastal jet can be shown by the bottom pressure torque (BPT) (Holland, 1973) in the balance of the depth-integrated vorticity equation (Ezer and Mellor, 1994),

$$\frac{\partial}{\partial t}\left(\frac{\partial VD}{\partial x}-\frac{\partial UD}{\partial y}\right)+\nabla\times \mathrm{NL}+\left(\frac{\partial fUD}{\partial x}+\frac{\partial fUD}{\partial y}\right) -\left(\frac{\partial P_{\mathrm{b}}}{\partial x}\frac{\partial D}{\partial y}-\frac{\partial P_{\mathrm{b}}}{\partial y}\frac{\partial D}{\partial x}\right)-\left(\frac{\partial \mathrm{ts}_y}{\partial x}-\frac{\partial \mathrm{ts}_x}{\partial y}\right) +\left(\frac{\partial \mathrm{tb}_y}{\partial x}-\frac{\partial \mathrm{tb}_x}{\partial y}\right)=0, \quad (4)$$

where $(U,\ V)$ are depth-integrated velocities. It is convenient to show the term balance in (4) by placing all terms on the left side of the equation. However, caution should be taken for the signs in the referred terms in (4). The terms from the left to the right of (4) are the tendency term, the advection and diffusion term (dominated by the advection term), the Coriolis term, the BPT term, the surface and bottom stress curl terms. The bottom pressure P_{b} is defined as

$$P_{\mathrm{b}}=\rho_0 g\eta+g\int_{-H}^{0}\rho\,\mathrm{d}z \quad (5)$$

and the BPT can be expressed as

$$-\mathrm{curl}_z(P_{\mathrm{b}}\nabla D) \quad (6)$$

representing torque arising from the curl of the bottom pressure across the isobaths. As does the

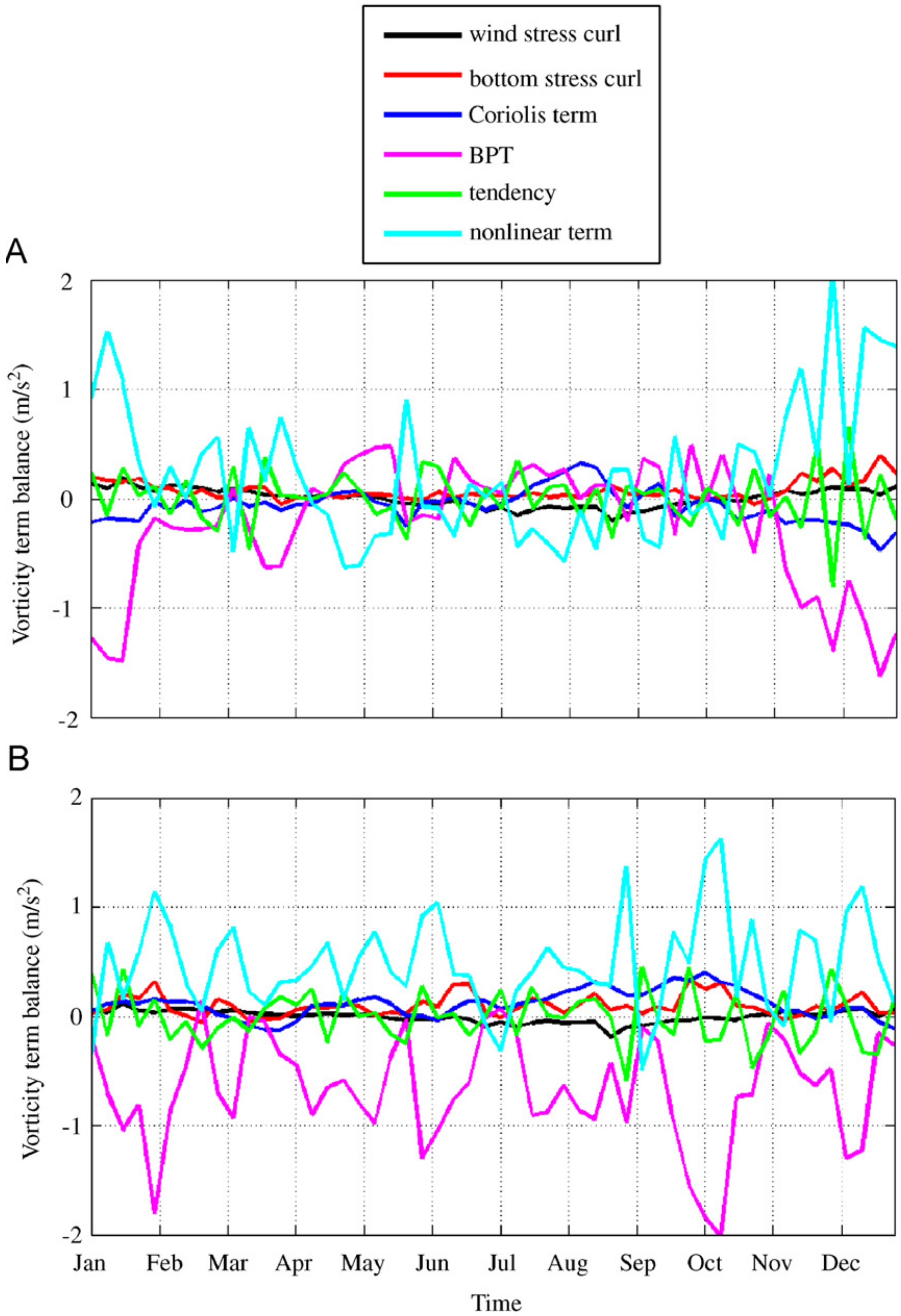

Fig. 12. Time series of the three-year average terms of the depth-integrated vorticity Eq. (4) at stations A and B ($\mathrm{m\,s^{-2}}$, multiplied by 10^8).

wind stress curl, this local forcing over the shelf of highly variable depth causes vorticity input. The time series of three-year average of terms in (4) at A and B are presented in Fig. 12. Overall, the dominant vorticity balances in the jet are between the BPT and nonlinear advection. The stress curls at both surface and bottom play little role in the balances. At the shelf station A, the positive BPT in Period 1 and the negative BPT in Period 2 are balanced primarily by the respective nonlinear advection terms, which impart negative and positive vorticity into the jet in Period 1 and Period 2, respectively. Since the vorticity between the jet and the coast is positive in Period 1 and negative in Period 2 when the jet is northward and southward, respectively, the vorticity inputs by the BPT term at A provide adverse vorticity, which, analogous to the role of adverse pressure gradient force, causes the vorticity between the jet and coast to be pushed toward the mainstream of the jet. Given that $\partial D/\partial x > \partial D/\partial y$, this is equivalent to saying that negative (positive) adverse vorticity is yielded because the force exerted by the slope over the shelf on the water to the north is stronger (weaker) than the slope to the south at A in the summer (winter). The adverse vorticity tends to form an adverse current next to the coast that is directed opposite to the direction of the jet (or weakens the jet), thus providing favorable conditions for separation of the jet (Gan et al., 1997). On the other hand, the Coriolis term, which contains the $\beta(\mathrm{d}f/\mathrm{d}y)$ effect and flow convergence, also plays a favorable but much weaker role in the coastal jet separation when northeastward and southward jets are strong in the summer (July and August) and winter (November to February), respectively. Similar to the results of Holland (1973), the magnitude of the BPT is amplified at the shelf edge of B as the slope of shelf is approached. The BPT is negative at all times and provides positive vorticity in the flow at this station. Away from the shear layer next to the coast and around the jet core, the vorticity inputs from the BPT at B tends to steer the jet northwestward after its separation at A during Period 1 and southwestward during Period 2.

The analyses of both momentum and vorticity balances evidently indicate that the force that leads to the jet separation is formed as a result of the interactions between the wind-driven coastal currents and shelf topography in the nearshore waters. Both the adverse pressure gradient and the adverse vorticity over the relatively shallow shelf topography serve to push the shear layer between the jet core and coast toward the mainstream of the jet for the jet separation.

5.3. Domain average momentum balance

It is informative to obtain overall dynamic condition in the SSCS by the time series of the area and upper-200 m averages of terms in (3) for R1 and R2 (Fig. 13). In x and y directions, the balances are

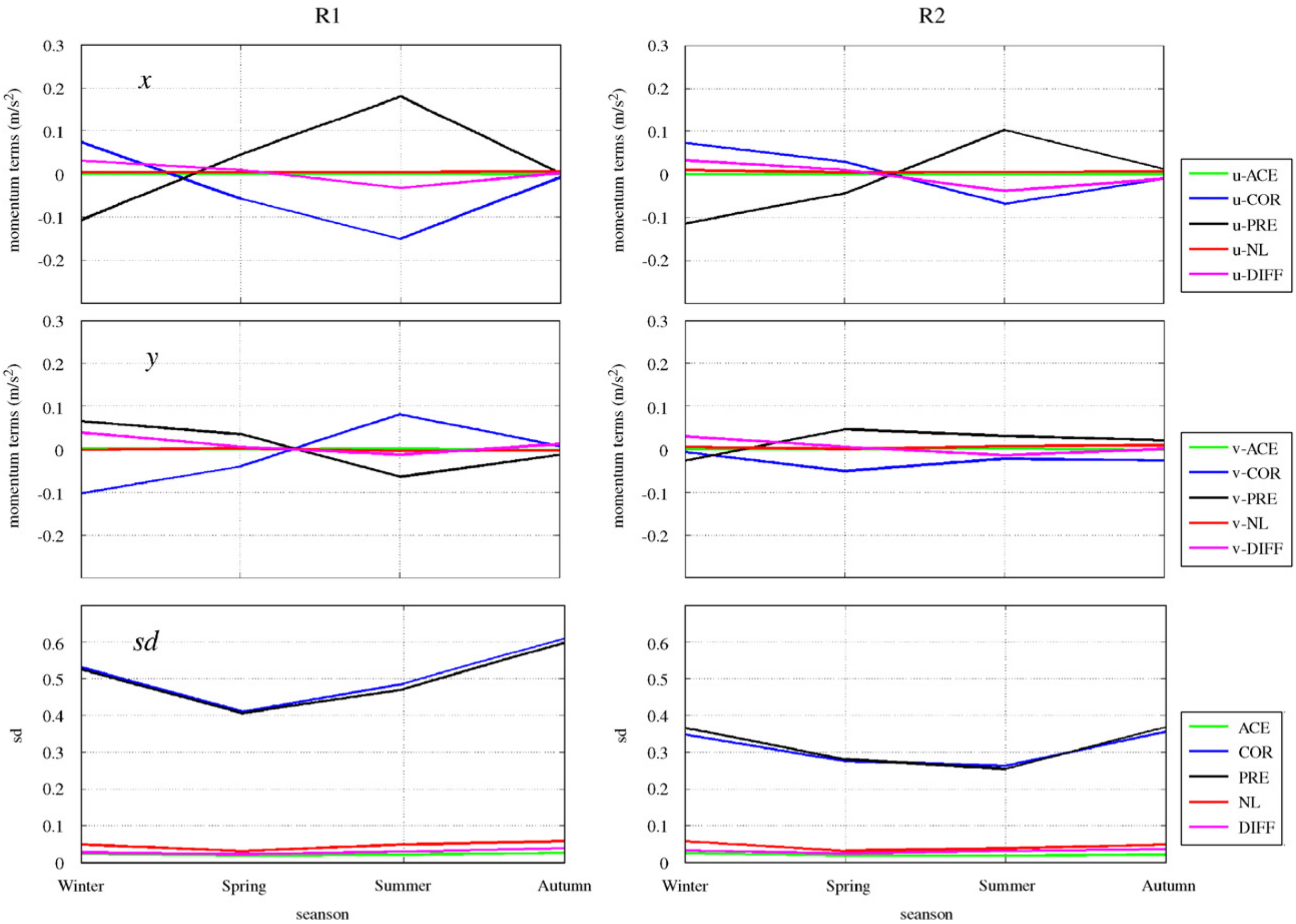

Fig. 13. Seasonal time series three-year average pressure gradient (PRE), Coriolis force (COR), acceleration (ACE), nonlinear advection (NL), vertical diffusion (DIFF) in the upper 200 m depth-averaged momentum equations in both x and y directions (m s^{-2}, multiplied by 10^5 and divided by water depth) in R1 and R2.

primarily between the pressure gradient and Coriolis terms, but modulated by vertical viscous term in both R1 and R2 in the winter and summer. The variance in the flow field is mainly from variability in the geostrophic currents which, as shown in this study, are regulated by the processes of coastal jet separation. In the x direction of R1, average geostrophic currents flow northward most of time except in the winter, reflecting the seasonal variation of the coastal jet in R1 (also see Fig. 6). In the balance of the y direction, the average geostrophic currents flow eastward from summer to early fall and westward during the other time of year, representing the separation of the coastal jet and onshore flux in R1 during these two respective periods.

In R2, although the nature of balances in the x direction is very similar to that in R1, the average current in the spring is weak and directed southward, opposite to the condition in R1, as the jet at this time is located beyond R2. The persistent westward component of currents in R2, as suggested by the Coriolis term in the y direction, may represent the circulation in the southern part of the anticyclonic eddy in the summer and westward shifting of the southward jet after its separation in the winter. Similar to the spatial distribution of seasonal stds in Fig. 6, it is found that the strongest flow variability occurs in the fall during the summer-winter transition in both R1 and R2. In R1, magnitudes of the std during the winter and summer are close; they are contributed mainly by the strong variances in the coastal jet as well as in shoreward currents in the winter and in the seaward separated currents in the summer. However, the stds in R2 during the winter are larger than those in the summer because of the southward separation of the coastal jet and cyclonic eddy in the winter.

6. Summary

A three-dimensional circulation model, together with evidence derived from satellite altimetry measurements, has been utilized to investigate the circulation variability and associated dynamic processes in the SSCS. The model is forced with high-frequency, time-dependent atmospheric forcing calculated from the NCEP reanalysis data and with time- and space-dependent lateral fluxes from the Pacific Ocean model. It is found that seasonal circulation in the SSCS is characterized by the southward and northeastward coastal jet separation from the coastal promontory off central Vietnam in the winter and summer, respectively. The cyclonic eddy in the summer and the anticyclonic eddy in the winter are formed in the respective regions to the east and to the southeast off central Vietnam as a result of the coastal jet separation. The variability of the circulation in the SSCS is created largely by the variability in the coastal jet and circulation associated with coastal jet separation. Strong variability exists along the track of the coastal jet next to the coast, as well as in R1 and R2 around the anticyclonic and cyclonic eddies induced by the jet separation in the summer and winter, respectively. The current variability also exists in the spring but with relatively small magnitude. Strong flow variability is found in both R1 and the northern part of R2 in the fall as a result of intensifying/weakening southward/northward jets during this summer–winter transition period.

The wind variability imparted to the oceanic flow field occurs mainly along the coastal jet by strong variance of the wind stress curl next to the coast and in the upper layer offshore in R1 by the variance of the wind stress. There is little direct correlation between the wind and flow variability in R2 although the strong variability of the negative wind stress curl next to the coast is expected to modulate the strength of the southward coastal jet in the winter and, thus, its separation. Overall, the simulated results agree reasonably well with those derived from the satellite altimetry measurements.

It is found that the northeastward and southward separation of the wind-induced coastal jet in the summer and winter, respectively, is associated with the formation of an adverse pressure gradient force or an adverse vorticity downstream of the jet in the nearshore waters around the coastal promontory at 12 °N. The adverse pressure gradient force is balanced by the prevailing wind stress in the summer and by the wind stress and nonlinear advection in the winter. On the other hand, the adverse vorticity over the shelf is induced primarily by the BPT, which represents the curl of the bottom pressure across the isobaths exerted by the shelf topography on the waters. The BPT is balanced by the nonlinear advection term. The adverse pressure gradient force or adverse vorticity is set-up by the monsoonal wind stress over the shallow shelf topography, which pushes the shear layer between the jet and coast toward the mainstream of the jet and leads to the separation of the jet. Combined with the finding that the separation can occur without the existence of a wind stress curl, it is clear that the interaction between wind-driven coastal currents and bottom topography in the nearshore waters, instead of wind stress curl alone, is one of the key factors controlling the coastal jet separation.

Acknowledgements

This research was supported by the Research Grants Council of Hong Kong under Grants CERG-601204, 601105 and 601006. Support to Qu was from the Japan Agency for Marine-Earth Science and Technology through its sponsorship of the International Pacific Research Center (IPRC contribution number 475). The authors would like to thank Y.Y. Cheung and X.P An for assistance in processing the data. The authors are grateful to Enrique Curchister of Columbia University for providing the output from the Pacific ocean model.

Appendix A. Open boundary conditions

The OBC adopted at the open boundaries in the model are described here. In this approach, the model solutions near the open boundaries are separated into local and global parts for all variables, i.e.

$$\phi = \phi_{\text{pacific}} + \phi_{\text{g}}, \tag{A1}$$

where ϕ is any of the dependent variables, and subscripts pacific and g denote the local and global solutions, respectively. The local solution is provided by the Pacific model and the global solution is obtained by subtracting the local solution from the total solution in the interior of the domain next to the open boundaries. By this, only the global solution is applied in the Sommerfeld radiation type OBC (Orlanski, 1976).

$$\frac{\partial \phi_{\text{g}}}{\partial t} + C_{\text{g}} \frac{\partial \phi_{\text{g}}}{\partial N} = 0, \tag{A2}$$

where C_{g} is the propagation speed of disturbance, t is time, and N is the coordinate normal to the open boundary. This approach is physically sensible since only the unforced part of the solution is applied to the radiation condition, which is based on an unforced local wave equation (A2). The speed of the disturbances at the open boundary is determined from (e.g., Chapman, 1985):

$$C_{\text{g}} = \frac{\phi^{n-1}_{\text{g}B\mp1} - \phi^{n+1}_{\text{g}B\mp1}}{\phi^{n+1}_{\text{g}B\mp1} + \phi^{n-1}_{\text{g}B\mp1} - 2\phi^{n}_{\text{g}B\mp2}}, \tag{A3}$$

where the upper and lower sign in $\mp$ are for the right and left boundaries, respectively. The solution at the open boundary is calculated separately for inflow and outflow conditions, in which the Pacific information influences the model solutions only during inflow conditions.

For inflow, $C_{(\text{g})} < 0$:

$$\phi^{n+1}_{B} = \phi^{n-1}_{B} - \frac{2\Delta t}{\lambda}[\phi^{n-1}_{B} - \phi^{n-1}_{\text{pacific}}]. \tag{A4}$$

For outflow, $C_{(rmg)} > 0$:

$$\phi^{n+1}_{B} = \phi^{n+1}_{\text{pacific}} + \phi^{n+1}_{\text{g}B}, \tag{A5}$$

where $\phi^{n+1}_{\text{g}B} = \phi^{n}_{\text{g}B\mp1}$ according to Camerlengo and O'Brien (1980). ϕ represents $(UA,\ u)$ $(VA,\ v)$, the potential temperature and salinity. A no-gradient condition is chosen for η in this study, where $\eta_B = \eta_{B\mp1}$. The parameter λ acts as a relaxation time scale in the inflow conditions and is chosen to be three days. In (A4), Δt is the time step of the model integration and is equal to 600 s for the internal mode and 600/30 s for the external mode. In addition, a weak spatial smoother is applied to the three-dimension global variables, $\phi_{\text{g}B}$, from (A5) so that the noise evolved from the radiation condition can be reduced. The OBCs are similar to Roed and Smedstad (1984), but apply to both barotropic and baroclinic variables.

References

Batchelor, G.K., 1967. An Introduction to Fluid Dynamics. Cambridge University Press, New York, 615 pp.

Blumberg, A.F., Mellor, G.L., 1987. A description of a three-dimensional coastal ocean circulation model. In: Heap, N. (Ed.), Three-Dimensional Coastal Ocean Models, vol. 4. AGU, Washington, D.C., pp. 208.

Camerlengo, A.L., O'Brien, J.J., 1980. Open boundary condition in rotating fluids. Journal of Computational Physics 35, 12–35.

Chao, S., Shaw, P., Wu, S., 1996. Deep water ventilation in the South China Sea. Dee-Sea Research I 43 (4), 445–466.

Chapman, D.C., 1985. Numerical treatment of across-shore open boundaries in a barotropic ocean model. Journal of Physical Oceanography 15, 1060–1075.

Chu, P., Chen, C., Lu, Y., Lu, S., 1998. Wind-driven South China Sea basin warm-core/cool core eddies. Journal of Oceanography 54, 347–360.

Chu, P.C., Edmons, N.L., Fan, C.W., 1999. Dynamical mechanisms for the South China Sea seasonal circulation and thermohaline variabilities. Journal of Physical Oceanography 29, 2971–2989.

Curchitser, E.N., Haidvogel, D.B., Hermann, A.J., Dobbins, E.L., Powell, T.M., Kaplan, A., 2005. Multi-scale modeling of the North Pacific Ocean: Assessment and analysis of simulated basin-scale variability. Journal of Geophysical Research 110, C11021, doi:10.1029/2005JC002902.

Ezer, T., Mellor, G.L., 1994. Diagnostic and prognostic calculations of the North Atlantic circulation and sea level using a sigma coordinate ocean model. Journal of Geophysical Research 99 (C7), 14159–14171.

Fang, W., Fang, G., Shi, P., Huang, Q., Xie, Q., 2002. Seasonal structure of upper layer circulation in the southern South China Sea from in situ observations. Journal of Geophysical Research 107(C11), 3202, doi:10.1029/2003JC001343.

Gan, J.P., Allen, J.S., 2005a. On open boundary conditions in a limited-area coastal model off Oregon. Part 1: response to idealized wind forcing. Ocean Modeling 8, 115–113, doi:10.1016/j.ocemod2003.12.006.

Gan, J.P., Allen J.S., 2005b. Modeling upwelling circulation off the Oregon coast. Journal of Geophysical Research 110, doi:10.1029/2004JC002692.

Gan, J.P., Ingram, R.G., Greatbatch, R., 1997. On the unsteady separation/intrusion of Gaspe Current and variability in Baie des Chaleurs, Modelling Studies. Journal of Geophysical Research 102, 15567–15581.

Gan, J.P., Ingram, R.G., Greatbatch, R., Baaren, T., 2004. Variability of circulation induced by the separation of Gaspe Current in Baie des Chaleurs: observational studies, Estuarine, Coastal and Shelf Sciences 61 (2004) 393–402.

Gan, J.P., Li, H., Curchitser, E.N., Haidvogel, D.B., 2006. Modeling South China Sea circulation: response to seasonal forcing regimes. Journal of Geophysical Research 111(C06034), doi:10.1029/2005JC003298.

Haidvogel, A.B., McWilliams, J.C., Gent, P.R., 1992. Boundary current separation in a quasigeostrophic eddy-resolving ocean circulation model. Journal of Physical Oceanography 22, 882–902.

Holland, W.R., 1973. Baroclinic and topographic influences on the transport in western boundary currents. Geophysical Fluid Dynamics 4, 187–210.

He, Z., Wang, D.X., Hu, J., 2002. Features of eddy kinetic energy and variations of upper circulation in the South China Sea. Acta Oceanologica Sinica 21, 305–314.

Huwang, C., Chen, S.A., 2000. Circulations and eddies over the South China Sea derived from TOPEX/Poseidon altimetry. Journal of Geophysical Research 105, 23943–23965.

Li, L., Nowlin, W.D., Su, J., 1998. Anticyclonic rings from the Kuroshio in the South China Sea. Deep-Sea Research I 45, 1469–1482.

Liu, Z., Yang, H., Liu, Q., 2001. Regional dynamics of seasonal variability in the South China Sea. Journal of Physical Oceanography 31, 272–284.

Liu, Q., Jiang, X., Xie, S.-P., Liu, W.T., 2004. A gap in the Indo-Pacific warm pool over the South China Sea in boreal winter: seasonal development and interannual variability. Journal of Geophysical Research 109, C07012, doi:10.1029/2003JC002179.

Metzger, E.J., Hurlburt, H., 1996. Coupled dynamics of the South China Sea, the Sulu Sea and the Pacific Ocean. Journal of Geophysical Research 101 (C5), 12331–12352.

Orlanski, I., 1976. A simple boundary condition for unbounded hyperbolic flows. Journal of Computational Physics 21, 251–269.

Qu, T., 2000. Upper layer circulation in the South China Sea. Journal of Physical Oceanography 30, 1450–1460.

Qu, T., Mitsudera, H., Yamagata, T., 2000. Intrusion of the North Pacific waters into the South China Sea. Journal of Geophysical Research 105, 6415–6424.

Qu, T., Du, Y., Gan, J., Wang, D., 2007. Mean seasonal cycle of isothermal depth in the South China Sea. Journal of Geophysical Research 112, C02020, doi:10.1029/2006JC003583.

Roed, L.P., Smedstad, O.M., 1984. Open boundary conditions for forced waves in a rotating fluid. SIAM Journal on Scientific and Statistical Computing 5, 414–426.

Shaw, P.T., 1991. The seasonal variation of the intrusion of the Philippine Sea water into the South China Sea. Journal of Geophysical Research 96, 821–827.

Shaw, P.T., Chao, S.Y., 1994. Surface circulation in the South China Sea. Deep-Sea Research 41, 1663–1683.

Shaw, P.T., Chao, S.Y., Fu, L.L., 1999. Sea surface height variations in the South China Sea from satellite altimetry. Oceanologica Acta 22, 1–17.

Shchepetkin, A.F., McWilliams, J.C., 2005. The regional ocean modeling system: a split-explicit, free-surface, topography following coordinates ocean model. Ocean Modelling 9, 347–404.

Signell, R.P., Gyer, W.R., 1991. Transient eddy formation around headlands. Journal of Geophysical Research 96, 2561–2575.

Wu, C.R., Shaw, P.T., Chao, S.Y., 1998. Seasonal and interannual variations in the velocity field of the South China Sea. Journal of Oceangraphy 54, 361–372.

Wyrtki, K., 1961. Physical oceanography of the southeast Asian waters, Scientific results of marine investigations of the South China Sea and the Gulf of Thailand, NAGA Report, Scripps Institution of oceanography, La Jolla, CA, vol. 2, 195 pp.

Xie, S., Xie, Q., Wang, D.X., Liu, W. T., 2003. Summer upwelling in the South China Sea and its role in regional climate variations. Journal of Geophysical Research 108(C8) 3261, doi: 10.1029/2003JC001867.

Xu, X.Z., Qiu, Z., Chen, H., 1982. The general descriptions of the horizontal circulation in the South China Sea. In: Proceedings of the 1980 Symposium on Hydrometology of the Chinese Society of Oceanology and Limnology, Science Press, Beijing, pp. 137–145. (in Chinese with English abstract).

Xue, H., Chai, F., Pettigrew, N., Xu, D., Shi, M., Xu, J., 2004. Kuroshio intrusion and the circulation in the South China Sea. Journal of Geophysical Research 109, C02017, doi:10.1029/2002JC001724.